CrystEngComm

ROYAL SOCIETY OF CHEMISTRY

PAPER

View Article Online
View Journal | View Issue

Cite this: *CrystEngComm*, 2024, **26**, 5165

Synthesis, chloride-ion diffusion mechanisms, and anisotropic sintering of 2D layered erbium oxychloride nanoplatelets†

Jingxiang Cheng, [ab] Malsha Udayakantha,[ab] Saul Perez-Beltran,[ab] Luis Carrillo,[ab] Wasif Zaheer,[ab] Lucia Zuin[c] and Sarbajit Banerjee *[ab]

Increasing interest in halide-ion batteries as a means of long-duration energy storage has led to intense recent interest in mechanisms of anion migration in periodic solids. Lanthanide oxyhalides crystallize in a richly diverse set of structures with well-separated halide-ion slabs and represent potential solid electrolytes of halide batteries. However, oxyhalides of later lanthanides are underexplored with regard to preparatory methods, structural preferences, defect energetics, and anion migration pathways. Here, we report a non-hydrolytic sol–gel condensation route to ligand-passivated single-crystalline ErOCl nanoplatelets, which crystallize in van der Waals layered SmSI and YOF structure types with reduced coordination of the lanthanide centers as compared to the PbFCl structure type preferred by early lanthanide oxyhalides. Pressure-less annealing in an argon ambient environment results in anisotropic sintering of the platelets with strongly preferred grain growth along the *ab* plane whilst retaining the thin platelet morphology. The preferred grain growth can be traced to strongly anisotropic chloride-ion migration along the *ab* plane of the bilayered van der Waals solid, which represents the primary mechanism of mass transport across grain boundaries. First-principles nudged elastic band simulations indicate that a low-energy intralayer chloride-ion migration pathway becomes accessible within the chloride-ion slab along the *ab* plane in the presence of chloride vacancies. The simulations demonstrate the promise of modulation anion conductivity through site-selective modification on the cation and anion lattices. These findings offer valuable insights into an important emerging class of halide electrolytes, illuminate fundamental mechanisms governing anion transport in 2D materials, and provide a blueprint for materials processing to achieve directional ion diffusion pathways.

Received 12th June 2024,
Accepted 28th August 2024

DOI: 10.1039/d4ce00585f

rsc.li/crystengcomm

Introduction

Emerging materials criticality concerns and the burgeoning demand for long-duration energy storage solutions have motivated the exploration of alternatives to lithium-ion batteries. Particular emphasis is placed on the diversification of battery supply chains and application at GWh scales required for energy arbitrage in entirely reimagined highly renewable grids.[1,2] Halide-ion batteries are an attractive construct with the potential to access high energy densities, orders of magnitude greater crustal abundance of halide charge carriers as compared to lithium, and avoidance of dendrite formation that has plagued metal anode battery chemistries.[3–9] However, as compared to Li-ion diffusion,[10–12] mechanisms for halide-ion migration in periodic solids remain underexplored.[3,13–15]

Lanthanide oxyhalides exhibit a diverse array of crystal structures characterized by well-separated halide-ion slabs,[16] which makes them promising candidates for solid electrolytes of halide-ion batteries. This promise is manifested in record halide ion diffusion coefficients recorded for lanthanide oxyiodides, oxybromides, and oxychlorides.[17–21] The well-separated halide slabs of these compounds are amenable to vacancy engineering, which enables facile anion transport. In addition to their capability for halide-ion conduction, lanthanide oxyhalides demonstrate excellent thermal stability, which makes them particularly well suited for high-temperature applications.[17,18,20,21] The large bandgap and low electronic conductivity of lanthanide oxyhalides are furthermore optimal for employment as solid electrolytes of halide batteries where it is imperative to separate ion and electron flows.[3,22,23] Such solid electrolytes

[a] *Department of Chemistry, Texas A&M University, College Station, TX 77843-3012, USA. E-mail: banerjee@chem.tamu.edu*
[b] *Department of Material Science and Engineering, Texas A&M University, College Station, TX 77843-3012, USA*
[c] *Canadian Light Source, University of Saskatchewan, Saskatoon, SK S7N 2V3, Canada*

† Electronic supplementary information (ESI) available. See DOI: https://doi.org/10.1039/d4ce00585f

can be paired with insertion or conversion electrodes with transition metal redox centers.[3,24]

Aliovalent alloying on the lanthanide cation sublattice is used to engender point defect formation and facilitate anion-plane conduction.[20] Recent work has demonstrated facile and versatile halide-ion mobility in the anion slabs of PbFCl-structured LaOI wherein topochemical halide-ion replacement is driven along a gradient of increasing hardness of anions from LaOI to LaOF whilst entirely preserving the tetragonal PbFCl crystal structure.[25]

In contrast to the tetragonal matlockite crystal structure ($P4/nmm$-D_{4h}^{7}) preferred by early lanthanides (La–Ho), the later lanthanide (Er–Lu) oxyhalides tend to adopt a layered rhombohedral $R\bar{3}m$–D_{3d}^{5} structure.[16,26,27] These structures have alternating hexagonally packed $(LnO)^{+}$ bilayers separated by hexagonally packed X^{-} layers (amenable even to cation insertion in their quasi van der Waals gap).[28] Mechanisms of halide-ion diffusion in these open-framework structures remain almost entirely unexplored. In this work, we report the synthesis of ligand-passivated ErOCl nanoplatelets through a non-hydrolytic sol–gel condensation reaction, examine mechanisms of chloride-ion diffusion, and demonstrate a surprising anisotropic sintering mechanism mediated by constrained chloride-ion diffusion along two-dimensional anion planes.

ErOCl is a dimorphic compound and crystallizes both in tetragonal and rhombohedral polymorphs. The rhombohedral structure, layered along the *c*-axis, features two polymorphs with different stacking sequences: ABC stacking corresponds to the SmSI structure type, whereas ACB stacking corresponds to the YOF structure type. Synthetic outcomes are typically a mix of both stacking sequences. In general, the synthesis of oxyhalides of later lanthanides is relatively poorly explored. Hydrochlorination of lanthanide oxides followed by hydrolysis yielded poorly crystalline mixtures of rhombohedral (YOF)/tetragonal[27] or SmSI/YOF structure types.[28] Annealing these mixtures at temperatures >750 °C for extended periods of time (2–7 weeks) using halide fluxes (LiCl/KCl/$ErCl_3$) to dissolve impurity phases has been reported to yield more crystalline materials. However, the products continued to be contaminated by Er_2O_3 and other unidentified phases.[27,29] Attempts to synthesize ErOCl by precipitation of ethanol dispersions of $ErCl_3$ with NH_4OH and subsequent calcination at 500 °C yielded amorphous products even though this synthesis provided a reliable path to obtaining oxyhalides of the early lanthanides (La–Ho) crystallized in the PbFCl structure.[30] ErOCl phases obtained with a similar approach where hydrated $ErCl_3$ was sintered started to oxidize to Er_2O_3 at 550 °C,[31] precluding further crystallization of SmSI/YOF-structured phases.

In this article, we devise a facile non-hydrolytic ligand-exchange and condensation route to prepare ErOCl nanocrystals crystallizing in the rhombohedral $R\bar{3}m$ space group without additional annealing. ErOCl nanoplatelets prepared by this method adopt a rhombohedral 2D layered $R\bar{3}m$ crystal structure with SmSI and YOF structure types. The prepared nanoplatelets are characterized by powder X-ray diffraction, transmission electron microscopy, Fourier transform infrared spectroscopy, and X-ray absorption near-edge structure (XANES) spectroscopy. High-temperature annealing of ErOCl results in anisotropic sintering into larger thin nanoplatelets, which we posit is mediated by 2D chloride-ion diffusion. Fundamental mechanisms of chloride-ion diffusion in these structures have been examined by first-principles density functional theory (DFT) calculations.

Experimental

Materials

Erbium(III) chloride ($ErCl_3$) (≥99.5%) and erbium(III) isopropoxide (herewith abbreviated as $Er(O^iPr)_3$) (≥99.5%) were purchased from Strem Chemicals, Inc. and used without further purification. Oleylamine (≥97%) was purchased from Millipore Sigma. Hexadecylamine (≥90%) and tetradecylamine (≥98%) were purchased from ThermoFisher Scientific. All the precursors were dried under a steady flow of N_2 overnight before use. Solvents used in synthesis include *n*-hexanes (anhydrous, 95%), ethanol (95%), and acetone (≥99.5%) from Millipore Sigma.

Synthesis and sintering of ErOCl nanoplatelets

ErOCl nanocrystals were prepared using a non-hydrolytic sol–gel reaction by the reaction of $ErCl_3$ with $Er(O^iPr)_3$ by adapting a synthetic scheme developed for earlier lanthanide oxyhalides.[16,25,32] In analogy with reaction mechanisms established for the synthesis of oxides, a proposed reaction pathway is envisioned wherein an initial ligand scrambling reaction yields haloalkoxides, which are subsequently condensed to form ErOCl.[33–35] Briefly, 2 mmol of $ErCl_3$ was combined with 2 mmol of $Er(O^iPr)_3$ in a three-neck round bottom flask inside an Ar glove box (O_2, H_2O <5 ppm). The three necks of the round bottom flask were secured with a rubber septum, a temperature probe, and an overhead condenser equipped with a gas inlet controller. The reaction was carried out under an Ar ambient environment in a Schlenk line using 5 mmol of oleylamine as the passivating ligand and coordinating solvent. Alternatively, the same reactions were repeated using 5 mmol of hexadecylamine and tetradecylamine instead of oleylamine as the coordinating solvent and passivating ligand. The reaction mixture was heated to 340 °C with continuous magnetic stirring. After 2 h of reaction, the reaction mixture was cooled and quenched to 80 °C by the addition of hexanes. The prepared nanoplatelets were precipitated by the addition of acetone. The final product was recovered and cleaned using several precipitation/resuspension cycles. Excess solvent was removed by washing with copious amounts of ethanol until the brown supernatant turned clear and colorless.

The nanoplatelets were sintered using an MTI GSL-1700 high-pressure tube furnace. As-prepared powders were placed in an alumina crucible, gently pressed to maintain contact,

and then heated at 1050 °C for a duration of 12 h at a controlled heating rate of 5 min °C^{-1} under a consistent Ar flow of 70 mL min^{-1}.

Characterization

Powder X-ray diffraction (XRD) patterns were acquired using a Bruker-AXS D8 Vario X-ray powder diffractometer with a Cu Kα radiation source (λ = 1.5418 Å) in the 2θ range from 5 to 60° at a step size of 0.003°. Simulations of powder XRD patterns were performed using GSASII.[36]

FTIR spectroscopy was performed using a Bruker Vertex-70 instrument with a Pike MIRacle single-reflection total attenuated reflectance (ATR) accessory.

Transmission electron microscopy (TEM) images were acquired using an FEI Tecnai G2 F20 ST instrument operated at an accelerating voltage of 200 kV. The ErOCl powder was dispersed in 2-propanol and then the solution was deposited onto 300-mesh carbon-coated Cu grids for high-resolution TEM (HRTEM).

Er $N_{4,5}$ X-ray absorption near-edge fine structure (XANES) spectra were concurrently acquired at the Variable Line Spacing-Plane Grating Monochromator (VLS-PGM) beamline of the Canadian Light Source with an energy resolution $E/\Delta E$ >10 000.[37] Powder samples were adhered to carbon tape and all spectra were recorded at room temperature, with a step size of 0.1 eV and a dwell time of 1 s in a sample chamber maintained below 1 × 10^{-8} Torr. In collecting XANES spectra, the total fluorescence yield (FLY)[38] was recorded with an MCP detector. All spectra recorded were normalized with respect to the incident photon flux (I_0), which in turn was recorded by monitoring the current emitted by a Ni mesh (90% transmission) located just upstream of the sample.

N K-edge XANES spectra were collected at the National Synchrotron Light Source II of Brookhaven National Laboratory beamline SST-1 operated by the National Institute of Standards and Technology. Measurements were performed in partial electron yield (PEY) mode with a nominal resolution of 0.1 eV. The PEY signal was normalized to the incident beam intensity of a clean gold grid to eliminate the effects of any incident beam fluctuations and optical absorption features.

First-principles calculations

Geometry optimizations were carried out using DFT as implemented in the Vienna *ab-initio* simulation package (VASP) for both SmSI and YOF polymorphs of ErOCl.[39,40] Brillouin zone integration was performed using a 4 × 4 × 1 Monkhorst–Pack mesh.[41] The projector-augmented wave formalism was used to capture electron–ion interactions. Electron exchange and correlation were addressed using the generalized gradient approximation based on the Perdew–Burke–Ernzerhof functional (PAW-GGA-PBE).[42–44] The electronic self-consistent loop and ionic relaxation loops were adjusted to below 10^{-5} and 10^{-4} eV, respectively.

Vacancy formation energies were determined by calculating the difference in total energy between the pristine structure and a modified structure with a vacancy. This vacancy was created by displacing the atom 3 Å from the topmost layer on the slab to avoid charge imbalance.[45–47] The vacancy formation energy E_F was calculated using the total energy per atom (n) from the pristine structure E_P subtracted by the total energy per atom (n) of the vacant structure E_V: $E_F = (E_P - E_F)/n$.

A single-point energy calculation was performed to calculate the projected density of state (pDOS) with Local Orbital Suite Toward Electronic-Structure Reconstruction (LOBSTER).[48,49] Bunge's description for the local basis functions was used for the pDOS calculation with 6s and 4f orbitals for erbium, 2s and 2p orbitals for oxygen, and 3s and 3p orbitals for chlorine.

The climbing-image nudged elastic-band (CI-NEB) method using a 288-atom supercell (14.88 Å × 12.88 Å × 27.15 Å) was used to calculate the migration barrier along the minimum energy pathway.[50] The same simulation parameters from geometry optimizations were applied except that the Brillouin zone integration grid was set to the Γ-point (1 × 1 × 1); the ionic optimization loop was used in conjunction with a force optimizer with a convergence criterion of 0.03 eV Å^{-1}.[51]

Results and discussion

Early lanthanide oxychlorides have a strong preference for the tetragonal matlockite PbFCl structure type[16] (Fig. 1A). In this structure type, $(LnO)^+$ slabs are separated by halide slabs. Lanthanide ions reside at the centers of mono-capped square antiprisms comprising four oxide ions in the underlying layer and four chloride-ions in an upper anion slab; a fifth more distant chloride-ion from the nearest-neighbor layer completes the nine-fold local coordination environment. As a result of lanthanide contraction, later lanthanides are no longer able to maintain a nine-coordinated ligand shell. As such, later lanthanides (Er–Lu) are crystallized in a rhombohedral crystal structure with a seven-fold (four oxides and three chlorides) coordination (Fig. 1B).[16] ErOCl, the first lanthanide in the series where the lower-symmetry structure-type can be stabilized is dimorphic with both tetragonal matlockite and rhombohedral $R\bar{3}m$–D^5_{3d} polymorphs being accessible.[26,27] In contrast to the tetragonal structure with 3D bonding mediated by La–Cl connectivity between the slabs (Fig. 1C), rhombohedral ErOCl is layered along the crystallographic *c*-axis (Fig. 1D). The separation between halide ions in adjacent layers is *ca.* 3.45 Å (which yields an interlayer spacing of *ca.* 2.56 Å). Er atoms reside at the centers of mono-capped trigonal antiprisms.[27,52] The rhombohedral structure adopts two polymorphs differentiated by distinctive stacking sequences along the crystallographic *c*-axis as depicted in Fig. 1D. The same Cl–Er–O–O–Er–Cl connectivity is manifested with the only distinction being the sequence of stacks: ABC stacking corresponds to the SmSI structure type, whereas ACB stacking emulates the YOF structure.

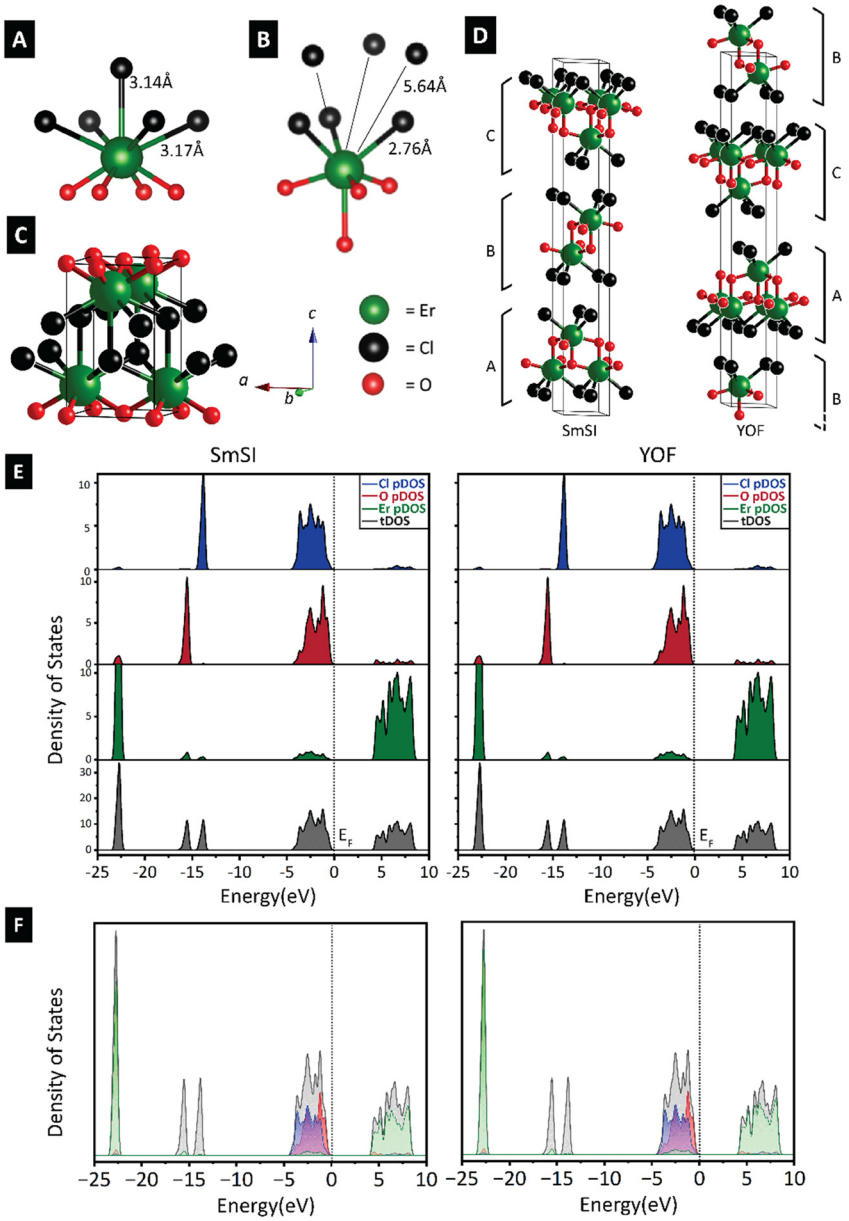

Fig. 1 Comparison of the Er local coordination geometry in (A) tetragonal and (B) rhombohedral crystal structures. Unit cells of (C) tetragonal PbFCl and (D) rhombohedral SmSI (left) and YOF (right) structure types viewed approximately parallel to the crystallographic *a*-axis. The figure contrasts ABC SmSI and ACB YOF stacking sequences. (E) Density of states plots of ErOCl in SmSI and YOF variants: total and projected DOS graphs of ErOCl in the SmSI variant (left) and YOF variant (right), (F) projected DOS graphs of SmSI and YOF variants contrasting the orbital contributions from Er 4f, O 2p, and Cl 3p orbitals.

First-principles DFT calculations of the total density of states (DOS) are plotted in Fig. 1E along with the atom-projected partial DOS. Fig. 1F plots the orbital-projected DOS (pDOS) for both stacking sequences. In both polymorphs, the conduction band is derived primarily from narrow erbium 4f contributions, whereas the valence band is derived primarily from chloride 3p and oxygen 2p-derived states. As is typical of a dimensionally confined van der Waals solid, the electronic structure is primarily governed by intralayer bonding in the bilayers with the bilayer stacking sequence having scarce little effect on the Fermi surface. The relative invariancy of the electronic structure points to the origins of the synthetic challenges in controlling the stacking sequence in homogeneous bulk synthesis given that the two polymorphs are closely spaced in energy.

As noted above, synthetic methods for the preparation of well-defined nanocrystals of rhombohedral ErOCl are rather sparse. Here, we adapt a synthetic methodology (Fig. 2A) based on non-hydrolytic sol–gel condensation to prepare well-defined nanoplatelets of ErOCl.[25,32] Our proposed reaction mechanism is analogous to non-hydrolytic sol–gel processes for metal oxides which proceed with the

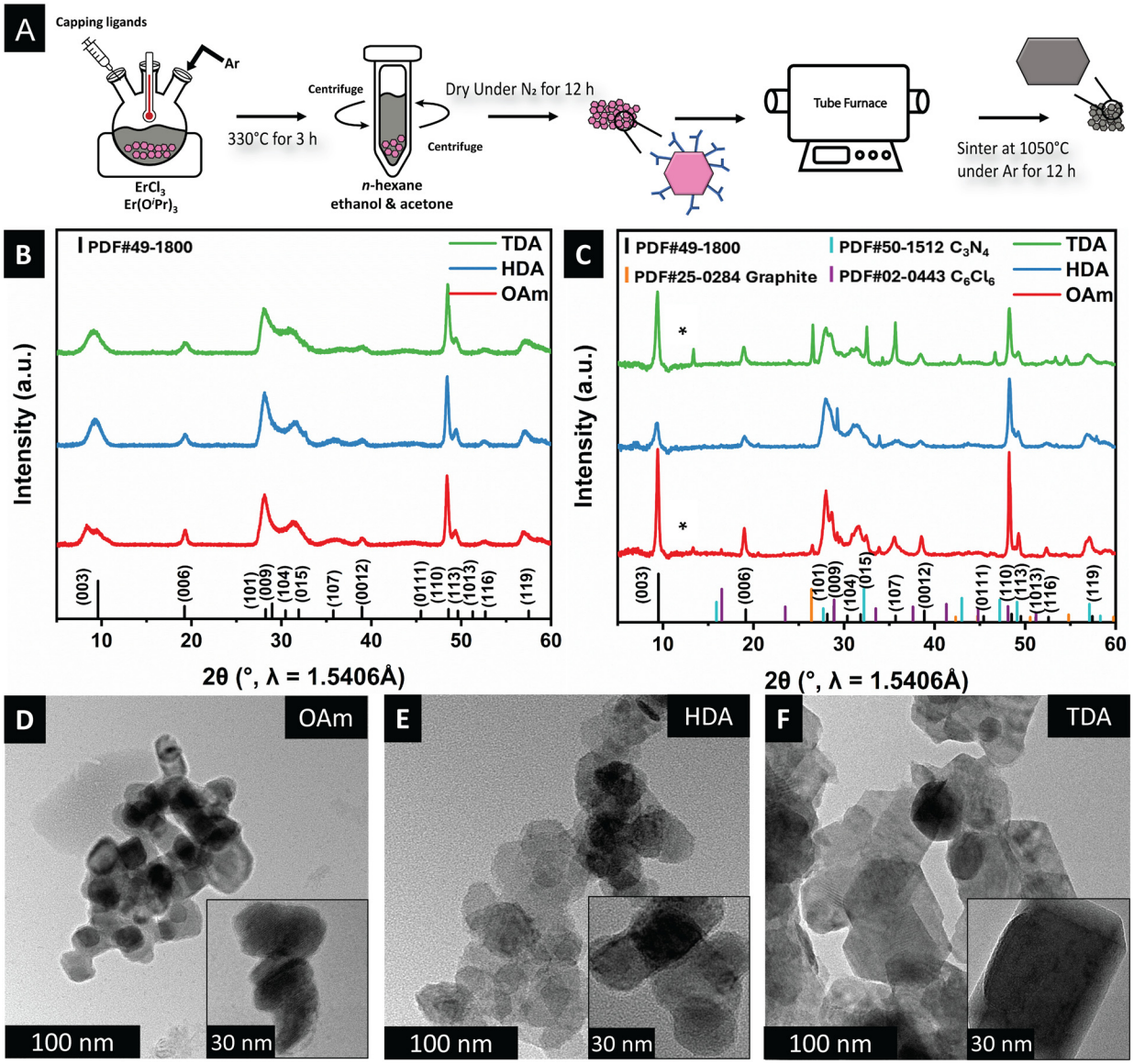

Fig. 2 (A) Schematic illustration of the synthesis and sintering of ErOCl nanoplatelets; (B) and (C) powder XRD patterns of ErOCl samples synthesized with OAm (red), HDA (blue), and TDA (green) indexed to an $R\bar{3}m$ unit cell (PDF# 49-1800, black ticks) before and after annealing at 1050 °C under an Ar environment, which are further indexed to graphite (PDF# 25-0284, orange ticks), carbon nitride (PDF# 50-1512, teal ticks), carbon chloride (PDF# 02-0443, purples ticks) and reflections resulting from the preferred orientation (black asterisks); (D–F) TEM images of OAm-, HDA-, and TDA-capped ErOCl nanocrystals. The insets show higher magnification images of the nanoplatelets.

elimination of alkyl halide or dialkyl ether.[34,35] Evidence for ligand scrambling as an initial step is derived from previous work on tetravalent alkoxides where the chain length and branching of the alkoxide precursor were systematically modified.[33] An initial erbium haloalkoxide is thought to be stabilized as per:

$$\mathrm{ErCl_3(soln.) + Er(O^iPr)_3(soln.) \rightarrow ErCl_{(3-x)}(O^iPr)_x(soln.) + ErCl_x(O^iPr)_{(3-x)}(soln.)} \quad (1)$$

Elimination of alkyl halide or dialkyl ether by the cross-condensation of mixed halo-alkoxides mediated by a proposed S_N1 pathway establishes the ErOCl framework as per:[53]

$$\mathrm{ErCl_{3-x}(O^iPr)_x(soln.) + ErCl_x(O^iPr)_{3-x}(soln.) \rightarrow (O^iPr)(Cl)–Er–O–Er–(Cl)(O^iPr)(soln.) + {}^iPrCl(soln.)} \quad (2)$$

$$\mathrm{ErCl_3(soln.) + (O^iPr)(Cl)–Er–O–Er–(Cl)(O^iPr)(soln.) \rightarrow 2ErOCl(s) + 3{}^iPrCl(soln.)} \quad (3)$$

An alternative E_1 elimination, ligand scrambling, and condensation route has also been suggested, which in this case would involve $ErCl(OH)(O^iPr)$ and $ErCl_2(OH)$ intermediates.[34,53]

Notably, in comparison with previous syntheses of PbFCl-structured early lanthanide oxyhalides,[25,54] a high molar excess of the amine coordinating solvent leads to

stabilization of ErOCl nanocrystals. Similarly, trials with trioctylphosphine oxide (TOPO) as the coordinating ligand led to similar preferential stabilization of oxides and mostly amorphous products (see Fig. S1†). The use of long-chain amines such as oleylamine as the coordinating solvent and passivating ligand at low molar excess (25 mmol to 5 mmol amine per 2 mmol $ErCl_3$) yields rhombohedral ErOCl.

Fig. 2B contrasts the powder XRD patterns of ErOCl synthesized with oleylamine (OAm), hexadecylamine (HDA), and tetradecylamine (TDA) as the capping ligands. In stark contrast to previous preparatory methods involving hydrochlorination of oxide followed by pyrohydrolysis, which yielded amorphous products with relatively poor long-range ordering,[27] our synthetic approach yields crystalline materials. The powder XRD patterns have been indexed to a trigonal $R\bar{3}m$ unit cell (PDF# 49-1800) corresponding to ($a = b = 3.7$ Å; $c = 27.6$ Å) for mixed SmSI/YOF structure types. Correspondence to the expected layered SmSI and YOF-type phases is seen in all the measured powder XRD patterns, with substantial splitting of the (003) reflection suggestive of significant layer disorder. No other crystalline products are recovered.

The ligand-passivated ErOCl nanocrystals have been annealed under an Ar atmosphere.[55] The powder XRD patterns of the annealed samples are shown in Fig. 2C. The relative intensities are modified selectively for the (003) and (110) reflections with respect to the other reflections. The strong growth of these reflections is suggestive of strongly anisotropic sintering. Fig. S2† displays simulated powder XRD patterns for differently constructed supercells for both YOF and SmSI structure types. Based on these simulations, the only powder XRD patterns that are consistent with the strong amplification of the (003) and (110) reflections are those that correspond to selective sintering along the *ab* plane, which results in extended X-ray coherent domains along this orientation. Fig. 2C shows that upon sintering, the XRD patterns include contributions from several by-products of the sintering process, such as graphite (C, PDF# 25-0284), carbon nitride (C_3N_4, PDF# 50-1512), and carbon chloride (C_6Cl_6, PDF# 02-0443), which are derived from sintering of the passivating ligands. Nevertheless, the reflections attributed to the SmSI phase are indicative of the preferred orientation along the *c*-axis, as corroborated by the simulated powder XRD patterns in Fig. S2.†

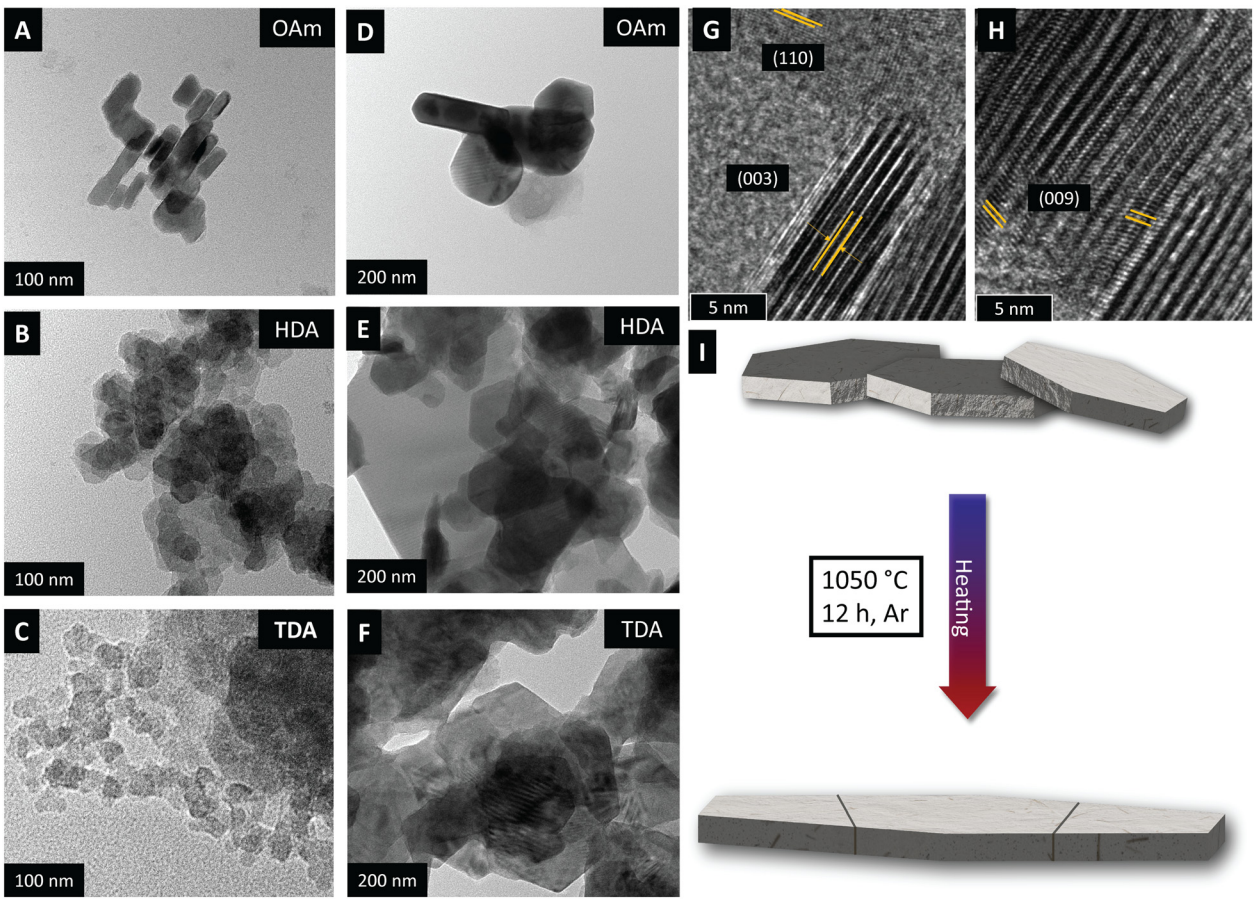

Fig. 3 (A–C) TEM images of as-synthesized OAm-, HDA-, and TDA-capped ErOCl nanoplatelets; (D–F) TEM images of OAm-, HDA-, and TDA-capped ErOCl after annealing at 1050 °C in an Ar ambient; environment (G and H) lattice-resolved high-resolution TEM images of OAm-capped ErOCl nanoplatelets before heating; (I) schematic illustration of anisotropic sintering upon annealing. The spacing between lattice planes is assigned to interplanar separations derived from PDF# 49-1800.

In Fig. 2D–F, prior to sintering, nanoplatelets are observed as individual platelets or agglomerates. The platelets adopt a mixture of hexagonal and rectangular morphologies. Notably, compared to prior studies on amine-capped early lanthanide oxychlorides,[32] the amine-capped ErOCl nanoparticles exhibited a more pronounced preferred orientation along the *ab* plane.

The TEM images obtained before and after annealing corroborate a similar trend, with the particle size growing significantly along the *ab* plane (Fig. 3A–F). Particles of ErOCl are fused along different directions,[56] resulting in faceted irregular-shaped particles that nevertheless retain their thin platelet morphology. The lattice-resolved HRTEM images of OAm-capped ErOCl before sintering (Fig. 3G and H) reveal distinct (110) and (003) planes, consistent with the simulated XRD patterns in Fig. S2,† which are indicative of anisotropic sintering along the *ab* plane as schematically illustrated in Fig. 3I.

In pressure-less sintering, the sintering rates along different crystallographic directions are dependent on both structural and geometric characteristics of the platelets.[57] In general, direction-dependent diffusion processes along particle surfaces modify the curvature of the particle surfaces, resulting ultimately in evolving grain boundary orientations in polycrystalline intermediates.[58] The directionality of sintering is governed by the grain boundary mass transfer or migration rates, which depend on the relative inclination and misorientation at grain boundaries. Given the strongly anisotropic crystal structure, mass transfer underpinning anisotropic sintering is likely to be governed by migration of the most mobile species, which in ErOCl are the chloride ions.[20] Chloride-ion diffusion in the *ab* plane thus yields extended thin platelets instead of 3D sintered solids. Notably, sintering hexagonal platelets manifest strongly preferred orientation of particles as desired for anisotropic ion diffusion. For instance, Youn and co-workers demonstrated strongly anisotropic proton migration in {0001} preferentially oriented hexagonal $Ba_5Er_2Al_2ZrO_{13}$ perovskite-structured solid electrolytes.[59] Controlling sintering directionality and anion conduction requires a detailed evaluation of chloride-ion diffusion mechanisms in these layered structures, which we describe in subsequent sections using first-principles simulations.

The Fourier transform infrared (FTIR) spectrum obtained for oleylamine-capped ErOCl nanocrystals is plotted alongside the spectrum measured for the oleylamine ligand in Fig. 4A. The broad band centered at 3300 cm^{-1} corresponds to symmetric and asymmetric stretching vibrations of the NH_2 group. Bands at 2926 and 2852 cm^{-1} are ascribed to asymmetric stretching modes of $-CH_3$ and $-CH_2-$ moieties. FTIR bands at 900–1000 and 650–900 cm^{-1} correspond to N–H bending and wagging modes, respectively.[28] Moreover, –C–N– bending (1078 cm^{-1}) and –C=C– bending (1073 cm^{-1}) modes can also be discerned.[52,55] Similarly, the FTIR spectra of hexadecylamine- and tetradecylamine-capped ErOCl demonstrate characteristic modes of HDA and TDA (Fig. S3†).

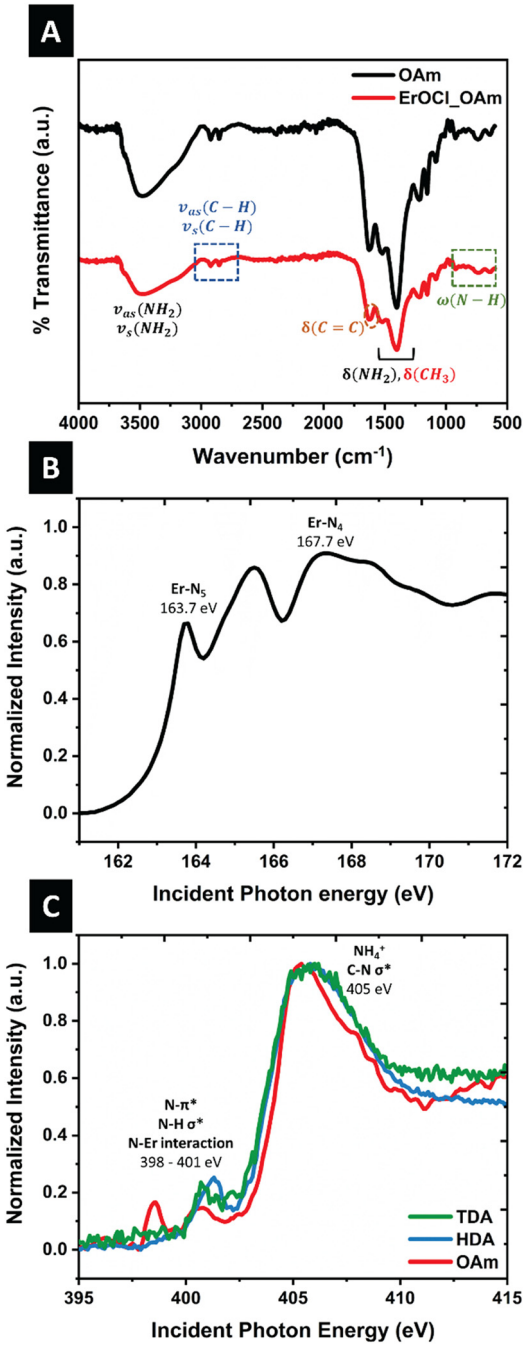

Fig. 4 (A) FTIR spectra of oleylamine (black) and OAm-capped ErOCl (red) depicting the role of oleylamine as a capping ligand. Note: ν = stretching vibrational modes; δ = bending vibrational modes; ω = wagging and scissoring modes. (B) X-ray absorption near edge structure spectrum acquired at Er $N_{4,5}$-edges. (C) X-ray absorption near edge structure spectra acquired at the N K-edge.

The Er $N_{4,5}$-edge XANES spectrum in Fig. 4B corresponds to excitation of core $4d_{3/2}$ (N_4-edge) and $4d_{5/2}$ (N_5-edge) electrons to the 4f levels of Er^{3+}. Preceding the giant resonance, three distinct features are assigned to multiplet splitting of 4d → 4f excitations. The $N_{4,5}$ edge absorption spectra of heavier lanthanide cations[60,61] are dominated by a combination of discrete $4d^{10}4f^n \rightarrow 4d^94f^{n+1}$ transitions.[62–64]

The N K-edge XAS spectra illustrated in Fig. 4C unveil multiple absorption features that are attributed to ligand-derived states.[65,66] The broad resonance in the vicinity of 405 eV can be attributed to NH_4^+ and C–N σ* interactions, reminiscent of spectral features measured for allylamine and propylamine.[65,67] The region spanning from 398 to 401 eV reflects amine–erbium, C–N π*, and N–H σ* interactions.[68,69] The observation of N–Er features, which are indicative of dative interactions involving nitrogen lone-pairs, provides insight into the mode of surface passivation. Specifically, the hybridization of nitrogen 2p lone-pair-derived slightly bonding LUMO states with Er states gives rise to both low-energy π* features and higher energy σ* features.

In order to evaluate the mechanisms governing anisotropic sintering, we next turn our attention to examining defect energetics and pathways for chloride-ion migration in ErOCl. We have evaluated chloride-ion migration considering three distinctive materials, an ordered ErOCl lattice, ErOCl with 10 at% Cl vacancies, and ErOCl with 10 at% Cl, 5 at% Er, and 3 at% O vacancies. Considering defect formation energies, Cl vacancies (0.042 eV per atom) have a substantially lower formation energy as compared to Er (0.111 eV per atom) and oxygen (0.078 eV per atom) vacancies, respectively. A strong preference for chloride vacancies over oxygen vacancies was previously evidenced for PbFCl-structured Eu-doped LaOCl in neutron activation analysis upon aliovalent substitution of divalent europium ions on trivalent lanthanum sites.[70]

Fig. 5A and B show that chloride-ion migration in non-defective ErOCl (rhombohedral SmSI structure type) proceeds within the same chloride plane. The diffusing anion adopts a triangular pyramid configuration with the closest Er atoms at the transition state; the closest Er ion is only 2.26 Å apart, whereas the other two adjacent Er ions are each at a distance of 3.41 Å. No significant structural deformation is observed beyond the first coordination sphere of the diffusing chloride ion. However, the migration barrier along this path is quite substantial, estimated to be 2.15 eV.

In contrast, randomly distributed 10 at% Cl vacancies in ErOCl afford access to an alternative lower-energy interlayer chloride-ion migration pathway (Fig. 5C and D). The transition state configuration for this migration path has the diffusing chloride ion interacting with multiple Er atoms from both layers at distances between 2.96 and 4.24 Å. The activation energy barrier for anion migration is reduced to 0.96 eV. Finally, for an ErOCl structure with 10 at% Cl, 5 at% Er, and 3 at% O vacancies, an interlayer chloride-ion migration path becomes accessible with an energy barrier of

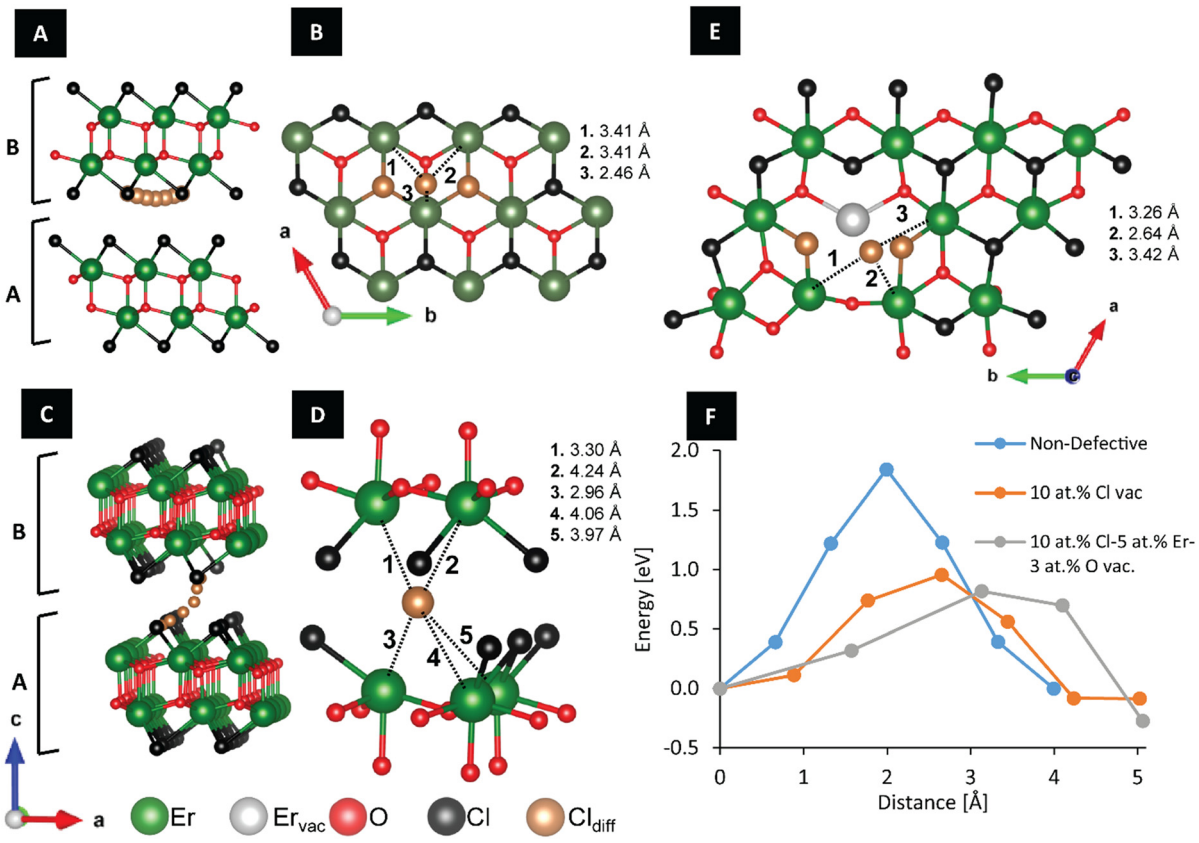

Fig. 5 Chloride-ion migration pathways: (A) and (B) chloride-ion migration pathway in non-defective ErOCl alongside a view of the chloride-ion coordination environment at the transition state. (C) and (D) Pathway for migration of chloride ions in ErOCl with 10 at% Cl vacancies and a view of the Cl coordination environment at the transition state. (E) Chloride-ion trajectory across in ErOCl with 10 at% Cl vacancies, 5 at% Er vacancies and 3 at% O vacancies. (F) Plots the activation energy barriers for the three chloride-ion diffusion paths.

0.82 eV. The Er vacancy leads to undercoordinated chloride ions being able to diffuse along the same Cl layer (Fig. 5E). In this configuration, the mobile chloride ion interacts with three distinctive Er ions at a distance of 3.26, 2.64, and 3.42 Å. Fig. 5F plots the energy barriers for these three distinctive modes of chloride-ion diffusion; the distance between images plotted in the horizontal axis shows that the presence of vacancies results in longer albeit lower energy chloride-ion migration pathways. As such, point defects such as those introduced through aliovalent alloying on the cation sublattice are critical to ensuring high chloride-ion mobility.[70] Videos S1A–S1C† provide animated views of the chloride-ion diffusion pathways. Chloride-ion diffusion along the *ab*-plane provides the primary mode of mass transfer during sintering and yields anisotropically sintered platelets.

Video S1† shows the top view of chloride-ion diffusion between layers A and B in non-defective ErOCl; Video S2† shows the side view of chloride-ion diffusion between layers A and B in ErOCl after 10 at% Cl vacancies; Video S3† shows the top view of diffusion on layer B in ErOCl with 10 at% Cl vacancies, 5 at% Er vacancies, and 3% at. O vacancies. In all three videos, Er atoms are colored green, Cl atoms are black, O atoms are red, and the diffusing Cl atom is distinguished as a dark orange sphere.

Conclusion

In summary, we report a low-temperature synthetic route to prepare ligand-passivated rhombohedral ErOCl nanoplatelets using a non-hydrolytic sol–gel condensation approach. Well-crystallized van der Waals solids crystallizing in the rhombohedral phase with YOF and SmSI stacking sequences are obtained when long-chain amines are used as coordinating solvents and passivating ligands. Synchrotron X-ray absorption spectroscopy results show specific bonding interactions between nitrogen from the amines and surface Er atoms. Chloride-ion vacancies are readily formed in this structure upon aliovalent doping on the cation sublattice, which further engenders chloride-ion mobility in this lattice. Pressure-less annealing results in anisotropic sintering of the platelets with strongly preferred grain growth along the *ab* plane whilst retaining the thin platelet morphology. The preferred grain growth can be traced to strongly anisotropic chloride-ion migration along the *ab* plane of the bilayered van der Waals solid.

Pathways and mechanisms of chloride-ion diffusion have been examined using first-principles nudged elastic band simulations, which indicate that an interlayer low-energy pathway becomes accessible along the *ab* plane in the presence of point defects. The results show a promising synthetic route to prepare van der Waals materials that can mediate anion diffusion. The DFT simulations demonstrate the promise of enhancing halide-ion mobility through site-selective modification on the cation and anion sublattice. Future work will focus on systematic aliovalent substitution on the cation sublattice and elucidation of the temperature-dependent chloride-ion conductivity of these materials.

Data availability

The data supporting this article have been included as part of the ESI.†

Author contributions

Conceptualization, J. C., M. U., S. P. B., and S. B.; methodology, J. C., M. U., and S. P. B.; investigation, J. C., M. U., S. P. B., L. C., L. Z., and W. Z.; data curation, J. C., M. U., and S. P. B.; writing – original draft, J. C., M. U., and S. P. B.; formal analysis, J. C., M. U. and S. P. B.; project administration S. B.; writing – review and editing, J. C., S. P. B., L. Z., and S. B.; validation, S. B.; supervision, S. B; funding acquisition, S. B.

Conflicts of interest

There are no conflicts to declare.

Acknowledgements

The authors would like to acknowledge support from Welch Foundation under award A-1978-20190330. Use of the Texas A&M Microscopy and Imaging Center is acknowledged. Portions of this research were conducted with the advanced computing resources provided by Texas A&M High Performance Research Computing. Part of the research described in this paper was performed at the VLS-PGM beamline at the Canadian Light Source, a national research facility of the University of Saskatchewan, which is supported by the Canada Foundation for Innovation (CFI), the Natural Sciences and Engineering Research Council (NSERC), the National Research Council (NRC), the Canadian Institutes of Health Research (CIHR), the Government of Saskatchewan, and the University of Saskatchewan. Part of the research described in this paper was performed at the National Synchrotron Light Source, Brookhaven National Laboratory, and was supported by the U.S. Department of Energy, Office of Basic Energy Science.

Notes and references

1 J. L. Andrews and S. Banerjee, It's not over until the big ion dances: potassium gets its groove on, *Joule*, 2018, **2**(11), 2194–2197.
2 J. W. Choi and D. Aurbach, Promise and reality of post-lithium-ion batteries with high energy densities, *Nat. Rev. Mater.*, 2016, **1**(4), 1–16.
3 X. Yang, B. Zhang, Y. Tian, Y. Wang, Z. Fu, D. Zhou, H. Liu, F. Kang, B. Li, C. Wang and G. Wang, Electrolyte design principles for developing quasi-solid-state rechargeable halide-ion batteries, *Nat. Commun.*, 2023, **14**(1), 925, DOI: **10.1038/s41467-023-36622-w**.
4 A. W. Xiao, G. Galatolo and M. Pasta, The case for fluoride-ion batteries, *Joule*, 2021, **5**(11), 2823–2844.
5 D. Zhang, K. Yamamoto, A. Ochi, Y. Wang, T. Yoshinari, K. Nakanishi, H. Nakano, H. Miki, S. Nakanishi and H. Iba, Understanding the reaction mechanism and performances

of 3d transition metal cathodes for all-solid-state fluoride ion batteries, *J. Mater. Chem. A*, 2021, **9**(1), 406–412.

6 F. Gschwind, G. Rodriguez-Garcia, D. Sandbeck, A. Gross, M. Weil, M. Fichtner and N. Hörmann, Fluoride ion batteries: Theoretical performance, safety, toxicity, and a combinatorial screening of new electrodes, *J. Fluorine Chem.*, 2016, **182**, 76–90.

7 V. K. Davis, C. M. Bates, K. Omichi, B. M. Savoie, N. Momčilović, Q. Xu, W. J. Wolf, M. A. Webb, K. J. Billings and N. H. Chou, Room-temperature cycling of metal fluoride electrodes: Liquid electrolytes for high-energy fluoride ion cells, *Science*, 2018, **362**(6419), 1144–1148.

8 M. A. Reddy and M. Fichtner, Batteries based on fluoride shuttle, *J. Mater. Chem.*, 2011, **21**(43), 17059–17062.

9 J. L. Andrews, E. T. McClure, K. K. Jew, M. B. Preefer, A. Irshad, M. J. Lertola, D. D. Robertson, C. Z. Salamat, M. J. Brady and L. F. Piper, Room-Temperature Electrochemical Fluoride (De) insertion into CsMnFeF6, *ACS Energy Lett.*, 2022, **7**(7), 2340–2348.

10 Z. Zhang and L. F. Nazar, Exploiting the paddle-wheel mechanism for the design of fast ion conductors, *Nat. Rev. Mater.*, 2022, **7**(5), 389–405.

11 P.-H. Chien, B. Ouyang, X. Feng, L. Dong, D. Mitlin, J. Nanda and J. Liu, Promoting Fast Ion Conduction in Li-Argyrodite through Lithium Sublattice Engineering, *Chem. Mater.*, 2023, **36**(1), 382–393.

12 B. J. Morgan, Mechanistic origin of superionic lithium diffusion in anion-disordered Li_6PS_5X argyrodites, *Chem. Mater.*, 2021, **33**(6), 2004–2018.

13 W. Zaheer, G. Agbeworvi, S. Perez-Beltran, J. L. Andrews, Y. Aierken, C. Weiland, C. Jaye, Y.-S. Yu, D. A. Shapiro and S. C. Fakra, Lessons learned from $FeSb_2O_4$ on stereoactive lone pairs as a design principle for anion insertion, *Cell Rep. Phys. Sci.*, 2021, **2**(10), 100592, DOI: **10.1016/j.xcrp.2021.100592**.

14 S. T. Hartman and R. Mishra, Layered electrides as fluoride intercalation anodes, *J. Mater. Chem. A*, 2020, **8**(46), 24469–24476.

15 J. D. Sundberg, D. L. Druffel, L. M. McRae, M. G. Lanetti, J. T. Pawlik and S. C. Warren, High-throughput discovery of fluoride-ion conductors via a decoupled, dynamic, and iterative (DDI) framework, *npj Comput. Mater.*, 2022, **8**(1), 106.

16 M. Udayakantha, P. Schofield, G. R. Waetzig and S. Banerjee, A full palette: Crystal chemistry, polymorphism, synthetic strategies, and functional applications of lanthanide oxyhalides, *J. Solid State Chem.*, 2019, **270**, 569–592.

17 N. Imanaka, M. R. I. B. Misran and N. Nunotani, Evidence for enormous iodide anion migration in lanthanum oxyiodide–based solid, *Sci. Adv.*, 2021, **7**(43), eabh0812.

18 K. Shitara, A. Kuwabara, K. Hibino, K. Fujii, M. Yashima, J. R. Hester, M. Umeda, N. Nunotani and N. Imanaka, Ionic conduction mechanism in Ca-doped lanthanum oxychloride, *Dalton Trans.*, 2021, **50**(1), 151–156, DOI: **10.1039/d0dt02502j**.

19 S. Tamura, Y. Kato and N. Imanaka, Ionic conducting properties in LaOCl–LaOBr solid solutions, *J. Alloys Compd.*, 2006, **408–412**, 653–656, DOI: **10.1016/J.JALLCOM.2004.12.069**.

20 N. Imanaka, K. Okamoto and G.-y. Adachi, Water-Insoluble Lanthanum Oxychloride-Based Solid Electrolytes with Ultra-High Chloride Ion Conductivity, *Angew. Chem., Int. Ed.*, 2002, **41**(20), 3890–3892, DOI: **10.1002/1521-3773(20021018)41:20<3890::AID-ANIE3890>3.0.CO;2-M**.

21 N. Imanaka and Y. Kato, Novel bromide anion conducting refractory solid electrolytes based on lanthanum oxybromide, *J. Mater. Sci.*, 2005, 6495–6498, DOI: **10.1007/s10853-005-1820-3**.

22 C. Wang, J. Liang, J. T. Kim and X. Sun, Prospects of halide-based all-solid-state batteries: From material design to practical application, *Sci. Adv.*, 2022, **8**(36), eadc9516, DOI: **10.1126/sciadv.adc9516**.

23 T. Famprikis, P. Canepa, J. A. Dawson, M. S. Islam and C. Masquelier, Fundamentals of inorganic solid-state electrolytes for batteries, *Nat. Mater.*, 2019, **18**(12), 1278–1291, DOI: **10.1038/s41563-019-0431-3**.

24 Q. Liu, Y. Wang, X. Yang, D. Zhou, X. Wang, P. Jaumaux, F. Kang, B. Li, X. Ji and G. Wang, Rechargeable anion-shuttle batteries for low-cost energy storage, *Chem*, 2021, **7**(8), 1993–2021.

25 M. Udayakantha, J. V. Handy, R. D. Davidson, J. Kaur, G. Villalpando, L. Zuin, S. Chakraborty and S. Banerjee, Halide Replacement with Complete Preservation of Crystal Lattice in Mixed-Anion Lanthanide Oxyhalides, *Angew. Chem., Int. Ed.*, 2021, **60**(28), 15582–15589, DOI: **10.1002/anie.202104231**.

26 D. H. Templeton and C. H. Dauben, Crystal Structures of Rare Earth Oxychlorides, *J. Am. Chem. Soc.*, 1953, **75**(23), 6069–6070, DOI: **10.1021/ja01119a535**.

27 E. Garcia, J. D. Corbett, J. E. Ford and W. J. Vary, Low-Temperature Routes to New Structures for Yttrium, Holmium, Erbium, and Thulium Oxychlorides, *Inorg. Chem.*, 1985, **24**(4), 494–498.

28 K. Song and S. M. Kauzlarich, New Intercalation Compounds of Layered Lanthanide Oxychlorides LnOCl (Ln = Ho, Er, Tm, and Yb) with Pyridine and Substituted Pyridines, *Chem. Mater.*, 1994, **6**(4), 386–394, DOI: **10.1021/cm00040a010**.

29 H. P. Beck, Oxychlorides of the Heavy Rare Earth Elements, *Z. Naturforsch., B: Anorg. Chem., Org. Chem.*, 1976, **31**(12), 1562–1564.

30 B. Terlingen, R. Oord, M. Ahr, E. Hutter, C. Van Lare and B. M. Weckhuysen, Mechanistic Insights into the Lanthanide-Catalyzed Oxychlorination of Methane as Revealed by Operando Spectroscopy, *ACS Catal.*, 2021, **11**(16), 10574–10588, DOI: **10.1021/acscatal.1c00393**.

31 W. W. Wendlandt, The thermal decomposition of the heavier rare earth metal chloride hydrates, *J. Inorg. Nucl. Chem.*, 1959, **9**(2), 136–139, DOI: **10.1016/0022-1902(59)80072-5**.

32 K. R. Kort and S. Banerjee, Shape-controlled synthesis of well-defined matlockite LnOCl (Ln: La, Ce, Gd, Dy) nanocrystals by a novel non-hydrolytic approach, *Inorg. Chem.*, 2011, **50**(12), 5539–5544, DOI: **10.1021/ic200114s**.

33 S. W. Depner, K. R. Kort and S. Banerjee, Precursor control of crystal structure and stoichiometry in twin metal oxide nanocrystals, *CrystEngComm*, 2009, **11**(5), 841, DOI: **10.1039/b819948p**.

34 J. Joo, T. Yu, Y. W. Kim, H. M. Park, F. Wu, J. Z. Zhang and T. Hyeon, Multigram Scale Synthesis and Characterization of

Monodisperse Tetragonal Zirconia Nanocrystals, *J. Am. Chem. Soc.*, 2003, **125**(21), 6553–6557, DOI: **10.1021/ja034258b**.

35 A. Vioux, Nonhydrolytic Sol-Gel Routes to Oxides, *Chem. Mater.*, 1997, **9**(11), 2292–2299.

36 J. H. O'Donnell, R. B. Von Dreele, M. K. Chan and B. H. Toby, A scripting interface for GSAS-II, *J. Appl. Crystallogr.*, 2018, **51**(4), 1244–1250.

37 Y. F. Hu, L. Zuin, G. Wright, R. Igarashi, M. McKibben, T. Wilson, S. Y. Chen, T. Johnson, D. Maxwell and B. W. Yates, *et al.*, Commissioning and performance of the variable line spacing plane grating monochromator beamline at the Canadian Light Source, *Rev. Sci. Instrum.*, 2007, **78**(8), 083109, DOI: **10.1063/1.2778613**.

38 M. Kasrai, Z. Yin, G. M. Bancroft and K. H. Tan, X-ray fluorescence measurements of X-ray absorption near edge structure at the Si, P, and S L edges, *J. Vac. Sci. Technol., A*, 1993, **11**(5), 2694–2699, DOI: **10.1116/1.578628**.

39 G. Kresse and J. Hafner, Ab initio molecular dynamics for open-shell transition metals, *Phys. Rev. B: Condens. Matter Mater. Phys.*, 1993, **48**(17), 13115–13118, DOI: **10.1103/physrevb.48.13115**.

40 G. Kresse and J. Furthmüller, Efficient iterative schemes for ab initio total-energy calculations using a plane-wave basis set, *Phys. Rev. B: Condens. Matter Mater. Phys.*, 1996, **54**(16), 11169–11186, DOI: **10.1103/PhysRevB.54.11169**.

41 H. J. Monkhorst and J. D. Pack, Special points for Brillouin-zone integrations, *Phys. Rev. B: Solid State*, 1976, **13**(12), 5188–5192, DOI: **10.1103/PhysRevB.13.5188**.

42 P. E. Blöchl, Projector augmented-wave method, *Phys. Rev. B: Condens. Matter Mater. Phys.*, 1994, **50**(24), 17953–17979, DOI: **10.1103/PhysRevB.50.17953**.

43 G. Kresse and D. Joubert, From ultrasoft pseudopotentials to the projector augmented-wave method, *Phys. Rev. B: Condens. Matter Mater. Phys.*, 1999, **59**(3), 1758–1775, DOI: **10.1103/physrevb.59.1758**.

44 J. P. Perdew, K. Burke and M. Ernzerhof, Generalized Gradient Approximation Made Simple, *Phys. Rev. Lett.*, 1996, **77**(18), 3865–3868, DOI: **10.1103/PhysRevLett.77.3865**.

45 R. Qiu, H. Lu, B. Ao, L. Huang, T. Tang and P. Chen, Energetics of intrinsic point defects in aluminium via orbital-free density functional theory, *Philos. Mag.*, 2017, **97**(25), 2164–2181.

46 T. Korhonen, M. J. Puska and R. M. Nieminen, Vacancy-formation energies for fcc and bcc transition metals, *Phys. Rev. B: Condens. Matter Mater. Phys.*, 1995, **51**(15), 9526.

47 C. J. Bartel, Review of computational approaches to predict the thermodynamic stability of inorganic solids, *J. Mater. Sci.*, 2022, **57**(23), 10475–10498.

48 C. T. Nelson, B. Winchester, Y. Zhang, S.-J. Kim, A. Melville, C. Adamo, C. M. Folkman, S.-H. Baek, C.-B. Eom and D. G. Schlom, *et al.*, Spontaneous Vortex Nanodomain Arrays at Ferroelectric Heterointerfaces, *Nano Lett.*, 2011, **11**(2), 828–834, DOI: **10.1021/nl1041808**.

49 S. Maintz, V. L. Deringer, A. L. Tchougréeff and R. Dronskowski, LOBSTER: A tool to extract chemical bonding from plane-wave based DFT, *J. Comput. Chem.*, 2016, **37**(11), 1030–1035, DOI: **10.1002/jcc.24300**.

50 G. Henkelman, B. P. Uberuaga and H. Jónsson, A climbing image nudged elastic band method for finding saddle points and minimum energy paths, *J. Chem. Phys.*, 2000, **113**(22), 9901–9904, DOI: **10.1063/1.1329672**.

51 D. Sheppard, R. Terrell and G. Henkelman, Optimization methods for finding minimum energy paths, *J. Chem. Phys.*, 2008, **128**(13), 134106, DOI: **10.1063/1.2841941**.

52 D. A. Odink, K. Song and S. M. Kauzlarich, Intercalation of pyridine into the layered samarium sulfide iodide (SmSI) structure of ytterbium oxide chloride (YbOCl), *Chem. Mater.*, 1992, **4**(4), 906–911.

53 R. Pokratath, D. Van Den Eynden, S. R. Cooper, J. K. Mathiesen, V. Waser, M. Devereux, S. J. L. Billinge, M. Meuwly, K. M. Ø. Jensen and J. De Roo, Mechanistic Insight into the Precursor Chemistry of ZrO_2 and HfO_2 Nanocrystals; towards Size-Tunable Syntheses, *JACS Au*, 2022, **2**(4), 827–838, DOI: **10.1021/jacsau.1c00568**.

54 G. R. Waetzig, G. A. Horrocks, R. D. Davidson, J. W. Jude, G. V. Villalpando, L. Zuin and S. Banerjee, In a Different Light: Deciphering Optical and X-ray Sensitization Mechanisms in an Expanded Palette of LaOCl Phosphors, *J. Phys. Chem. C*, 2018, **122**(28), 16412–16423, DOI: **10.1021/acs.jpcc.8b04291**.

55 S. Yang, A. Anderko, R. E. Riman and A. Navrotsky, Thermochemistry of 3D and 2D Rare Earth Oxychlorides (REOCls), *Inorg. Chem.*, 2022, **61**(19), 7590–7596, DOI: **10.1021/acs.inorgchem.2c00763**.

56 H. E. Exner and E. Arzt, *Sintering processes*, Springer, 1990.

57 E. Torresani, D. Giuntini, C. Zhu, T. Harrington, K. Vecchio, A. Molinari, R. K. Bordia and E. A. Olevsky, Anisotropy of mass transfer during sintering of powder materials with pore–particle structure orientation, *Metall. Mater. Trans. A*, 2019, **50**, 1033–1049.

58 S. Biswas, D. Schwen, H. Wang, M. Okuniewski and V. Tomar, Phase field modeling of sintering: Role of grain orientation and anisotropic properties, *Comput. Mater. Sci.*, 2018, **148**, 307–319.

59 Y. Youn, B. Hussain, A. Ullah, I. J. Hwang, J. Shin, J.-E. Hong, D. W. Joh, S.-B. Lee, R.-H. Song and S.-J. Park, Anisotropic Proton Migration in Hexagonal Perovskite-Related $Ba_5Er_2Al_2ZrO_{13}$ Oxide, *Chem. Mater.*, 2023, **35**(22), 9493–9504.

60 C. Dzionk, W. Fiedler and M. v. Lucke, Zimmermann, P. Photoion Spectroscopy in the 4 d Giant Resonances of the Lanthanides, *Phys. Rev. Lett.*, 1989, **62**(8), 878.

61 H. Ogasawara and A. Kotani, Calculation of rare-earth 4d giant-absorption spectra with multiplet effects and decay processes, *J. Synchrotron Radiat.*, 2001, **8**(2), 220–222.

62 E. Suljoti, Chemistry and Fundamental Electron Correlation in Chemically Prepared Lanthanide Nanoparticles, *Dissertation*, Staats-und Universitätsbibliothek Hamburg Carl von Ossietzky, 2008.

63 M. True, Fine structure in d-f and f-f transitions of Tm3+ and systematic investigation of 3d5-3d4 4s absorption of Mn2+ doped fluorides, *Dissertation*, Staats-und Universitätsbibliothek Hamburg Carl von Ossietzky, 2004.

64 E. Suljoti, M. Nagasono, A. Pietzsch, K. Hickmann, D. Trots, M. Haase, W. Wurth and A. Föhlisch, Geometric and electronic structure of lanthanide orthophosphate nanoparticles determined with x-rays, *J. Chem. Phys.*, 2008, **128**(13), 134706, DOI: **10.1063/1.2876360**.

65 P. Leinweber, J. Kruse, F. L. Walley, A. Gillespie, K.-U. Eckhardt, R. I. R. Blyth and T. Regier, Nitrogen K-edge XANES – an overview of reference compounds used to identify 'unknown' organic nitrogen in environmental samples, *J. Synchrotron Radiat.*, 2007, **14**(6), 500–511, DOI: **10.1107/s0909049507042513**.

66 A. Vairavamurthy and S. Wang, Organic Nitrogen in Geomacromolecules: Insights on Speciation and Transformation with K-edge XANES Spectroscopy, *Environ. Sci. Technol.*, 2002, **36**(14), 3050–3056, DOI: **10.1021/es0155478**.

67 A. G. Shard, J. D. Whittle, A. J. Beck, P. N. Brookes, N. A. Bullett, R. A. Talib, A. Mistry, D. Barton and S. L. McArthur, A NEXAFS Examination of Unsaturation in Plasma Polymers of Allylamine and Propylamine, *J. Phys. Chem. B*, 2004, **108**(33), 12472–12480, DOI: **10.1021/jp048250f**.

68 D.-C. Sergentu and J. Autschbach, X-ray absorption spectra of f-element complexes: insight from relativistic multiconfigurational wavefunction theory, *Dalton Trans.*, 2022, **51**(5), 1754–1764.

69 M. Ekimova, M. Kubin, M. Ochmann, J. Ludwig, N. Huse, P. Wernet, M. Odelius and E. T. J. Nibbering, Soft X-ray Spectroscopy of the Amine Group: Hydrogen Bond Motifs in Alkylamine/Alkylammonium Acid–Base Pairs, *J. Phys. Chem. B*, 2018, **122**(31), 7737–7746, DOI: **10.1021/acs.jpcb.8b05424**.

70 G. R. Waetzig, G. A. Horrocks, J. W. Jude, G. V. Villalpando, L. Zuin and S. Banerjee, Ligand-Mediated Control of Dopant Oxidation State and X-ray Excited Optical Luminescence in Eu-Doped LaOCl, *Inorg. Chem.*, 2018, **57**(10), 5842–5849, DOI: **10.1021/acs.inorgchem.8b00234**.